PAPER

Temperature dependence of the vibrational spectrum of porphycene: a qualitative failure of classical-nuclei molecular dynamics†

Yair Litman,[a] Jörg Behler [ID] [b] and Mariana Rossi [ID] *[a]

The temperature dependence of vibrational spectra can provide information about structural changes of a system and also serve as a probe to identify different vibrational mode couplings. Fully anharmonic temperature-dependent calculations of these quantities are challenging due to the cost associated with statistically converging trajectory-based methods, especially when accounting for nuclear quantum effects. Here, we train a high-dimensional neural network potential energy surface for the porphycene molecule based on data generated with DFT-B3LYP, including pairwise van der Waals interactions. In addition, we fit a kernel ridge regression model for the molecular dipole moment surface. The combination of this machinery with thermostatted path integral molecular dynamics (TRPMD) allows us to obtain well-converged, full-dimensional, fully-anharmonic vibrational spectra including nuclear quantum effects, without sacrificing the first-principles quality of the potential-energy surface or the dipole surface. Within this framework, we investigate the temperature and isotopologue dependence of the high-frequency vibrational fingerprints of porphycene. While classical-nuclei dynamics predicts a red shift of the vibrations encompassing the NH and CH stretches, TRPMD predicts a strong blue shift in the NH-stretch region and a smaller one in the CH-stretch region. We explain this behavior by analyzing the modulation of the effective potential with temperature, which arises from vibrational coupling between quasi-classical thermally activated modes and high-frequency quantized modes.

1 Introduction

Porphycene, a structural isomer of free-base porphyrin, provides a unique example of double hydrogen transfer (DHT) in a multidimensional anharmonic potential-

[a] Fritz Haber Institute of the Max Planck Society, Faradayweg 4-6, 14195 Berlin, Germany. E-mail: rossi@fhi-berlin.mpg.de

[b] Universität Göttingen, Institut für Physikalische Chemie, Theoretische Chemie, Tammannstr. 6, 37077 Göttingen, Germany

energy surface (PES).[1] In the gas-phase, the most stable isomer at the PES corresponds to a *trans* state, where the hydrogen atoms within the cage are located on opposite sides, as shown in Fig. 1. The strong in-cage hydrogen bonds give rise to pronounced vibrational couplings which are evidenced, for example, by the extreme broadening and complex structure of the NH vibrational band.[2,3] The ability to enhance, deactivate or trigger hydrogen transfer events in this family of molecules has a potential impact on the fabrication of molecular machines and nanodevices.[4–6] Different strategies can be followed to achieve this control, for example modifying the electronic structure by addition of different substituents, altering the thermodynamic conditions, or using external stimuli.[7–10]

Addressing this system using computer simulations requires a reliable description of the PES beyond the harmonic approximation, a full-dimensional representation of the system, and the inclusion of nuclear quantum effects (NQEs). Neglecting any of these aspects may lead to results that are qualitatively incorrect, as we have shown for the room-temperature IR spectrum of porphycene and the double hydrogen transfer reaction rates in the deep tunneling regime in ref. 2. In this work, we investigate whether certain approximations, like classical nuclei or dimensionality reduction, can grasp the essential physical aspects that modulate the vibrational fingerprints of porphycene and its isotopologues at different temperature regimes. Due to the high dimensionality of this system, density-functional theory (DFT) allied to path-integral based approximations to quantum dynamics are the state-of-the-art methodologies that can be applied with a tractable computational cost.

Temperature-dependent changes in vibrational fingerprints often include quite subtle changes in peak shapes and positions.[11–15] Within trajectory-based methods, it is therefore necessary to ensure statistical convergence in order to achieve predictive results from simulation. The computational cost of the hundreds of thousands of force evaluations with a hybrid exchange–correlation functional for the hundreds of path-integral replicas necessary to bridge different temperature regimes presents a considerable challenge. Recent developments of different types of machine-learning potentials in the realm of atomistic simulations[16–22] can be used to overcome this computational cost.

In this paper, we report the training of a high-dimensional neural network potential[23,24] (HDNNP) based on data from density-functional theory (DFT) with

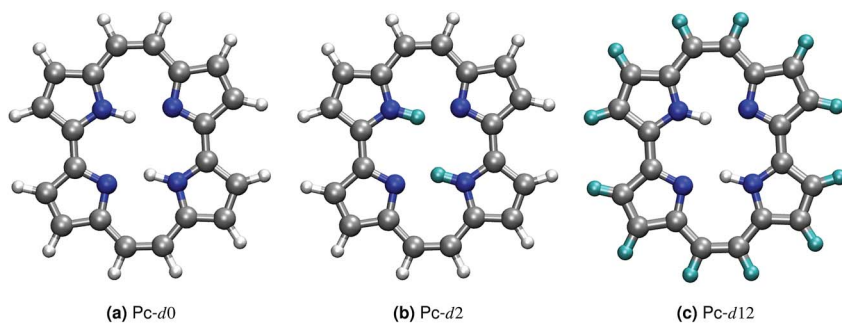**(a)** Pc-*d*0   **(b)** Pc-*d*2   **(c)** Pc-*d*12

Fig. 1 Depiction of the porphycene molecule in its gas-phase potential energy surface ground-state *trans* conformation. Atomic color code: hydrogen (white), carbon (grey), nitrogen (blue) and deuterium (cyan). The three isotopologues Pc-*d*0, Pc-*d*2 and Pc-*d*12 are shown in panels (a), (b) and (c).

a hybrid exchange–correlation functional (B3LYP[25–28]) and including pairwise van der Waals interactions.[29] We complement this potential by a Kernel Ridge Regression (KRR) model trained on the same *ab initio* calculations to reproduce the dipole moment of this molecule. This setup allows the classical-nuclei and path-integral-based molecular dynamics simulations to effortlessly reach the nanosecond time scale with *ab initio* accuracy. We address standard porphycene (Pc-*d*0), the isotopologue where the inner-cage hydrogens have been substituted by deuterium (Pc-*d*2), and the isotopologue where only the outer-cage hydrogens have been substituted by deuterium (Pc-*d*12) (see Fig. 1). These isotopologues have been the subject of previous experimental and theoretical work.[3,30–33] Based on the linear response time-correlation formalism, we compute the vibrational density of states and infrared spectra in a wide temperature range for the different isotopologues. We analyze their similarities and differences and address the relevance of including anharmonic contributions and nuclear-quantum effects in their full-dimensional nature, especially focusing on the NH-stretch signal which is the most puzzling feature of the vibrational spectrum of this molecule.

This manuscript is organized as follows: in Section 2.1 we present the details of the DFT calculations used to generate the data on which the HDNNP and the KRR are based. In Section 2.2, we provide a short theoretical background on the observables that we are going to compute. The training of the HDNNP potential and the KRR model, with the respective data set description and the validation tests are described in Sections 2.3 and 2.4 followed by the simulations protocol in Section 2.5. Having established a reliable description of our system we discuss our results for the temperature dependence of the vibrational spectra and the physical origins of the observed behaviors in Section 3. Finally, in Section 4, we close the manuscript summarizing our most important findings.

2 Methods

2.1 Electronic structure

The density-functional theory calculations were performed with the FHI-aims all-electron code.[34] According to previous benchmarks performed in ref. 2, the B3LYP functional including pairwise van der Waals (vdW) corrections yields a good agreement to benchmark-quality CCSD(T) reference data for stationary points on the PES, barrier heights and geometrical properties. In this manuscript, we used most of the data generated from the *ab initio* molecular dynamics trajectories in ref. 2 and augmented it by a few points, as detailed below, to train the HDNNP. We have therefore consistently used the *light* settings of the FHI-aims code package for all new calculations. For stationary points on the potential energy surface, we observed that *light* settings yield differences below 5 meV in relative energies and 0.005 Å in atomic distances (see ref. 2) with respect to *tight* settings. An assessment of the impact of different numerical grids and basis sets settings on the vibrational spectrum of porphycene is shown in Fig. S1 in the ESI.† We observe differences in peak positions of at most 20 cm^{-1} and minimal differences in the harmonic peak intensities.

2.2 IR spectrum and vibrational density of states

The IR spectrum and vibrational density of states presented in this paper were calculated within the linear-response time-correlation formalism. Within this

formalism, based on Fermi's golden rule,[35] the IR adsorption cross section $\sigma(\omega)$ is proportional to

$$\sigma(\omega) \propto \omega^2 \tilde{C}_{\mu\mu}(\omega), \tag{1}$$

where ω is the frequency, μ is the molecular dipole moment, and $\tilde{C}_{\mu\mu}(\omega)$ is the Fourier transform of the Kubo-transformed dipole–dipole time-correlation function.

The vibrational density of states is given by[36,37]

$$v\mathrm{DOS}(\omega) \propto \sum_{i=1}^{3N} \tilde{C}_{v_i v_i}(\omega), \tag{2}$$

where the index i runs through all $3N$ nuclear degrees of freedom in the system, and v_i is the velocity component of each degree of freedom. We note that the VDOS given in eqn (2) does not contain cross-terms involving the correlation of the velocities between different degrees of freedom, which instead contribute to the dipole spectrum.‡ The definition in eqn (2) is often connected to the incoherent dynamic structure factor in neutron scattering experiments[36,37] and obeys well-known sum rules.[38,39] The integral of the spectrum is proportional to the temperature,[39] such that in order to compare VDOS spectra at different temperatures, we have divided each one by their respective target temperature.

The time evolution of the dipole moment and the positions (and their derivatives) have been computed within the Born–Oppenheimer approximation with classical nuclei molecular dynamics (MD) and thermostatted ring-polymer molecular dynamics (TRPMD).[40] TRPMD is an approximation to nuclear quantum dynamics based on classical dynamics in the extended phase space of the ring polymer.[40,41] The methodology is very similar to ring-polymer molecular dynamics,[41] with the difference that the internal modes of the ring polymer are attached to thermostats, while the centroid follows Hamiltonian dynamics. Its connection to quantum dynamics has been shown as the short-time approximation to Matsubara dynamics.[42–44] There is a freedom in the choice of the thermostatting procedure,[40] and it has been recently shown that generalized Langevin equation (GLE) thermostats can be tailored to yield optimal spectra.[45] Here, we used the parameters proposed in ref. 45 for the GLE thermostats, which mitigate the spurious broadening of the TRPMD vibrational lineshape. The estimator for the dipole was computed as $\mu_P = \sum_{k=1}^{P} \mu_k / P$, where k runs over the P ring-polymer beads and μ_k is the dipole moment of the k-th replica. The estimator entering the vibrational density of states, due to the linearity of the velocity operator, is simply the velocity of the ring-polymer centroid. TRPMD is known to yield a good approximation to quantum time correlation functions that involve operators with a linear or almost linear dependence on positions. It does not capture nuclear quantum-mechanical coherence, and that can become more relevant at lower temperatures. We do not expect these effects to play a determinant role in the temperature range considered in the present study.

---

‡ This is easy to see if one would assume the dipole to be a linear function of the coordinates.

2.3 Potential energy surface from high-dimensional neural networks

High-dimensional neural network potentials as proposed by Behler and Parrinello[23] allow complex potential energy surfaces of very large systems containing thousands of atoms and all their associated degrees of freedom to be represented. In this approach the total energy E of the system is constructed as a sum of atomic energies E_i,

$$E = \sum_{i=1}^{N_{\mathrm{atom}}} E_i, \tag{3}$$

which depend on the local atomic environments up to a cutoff radius R_c, which typically has a value between 6 and 10 Å. The positions of all neighboring atoms inside these cutoff spheres are described by vectors of many-body atom-centered symmetry functions,[24] which incorporate the required translational, rotational and permutational invariance of the PES. These symmetry function vectors serve as inputs for individual atomic neural networks (NNs) yielding the E_i. For each element present in the system there is one atomic NN, *i.e.* the architectures and parameters of the atomic neural networks for a given chemical element are constrained to be the same, which is replicated as many times as there are atoms of the respective element. The parameters of the atomic NNs are determined in an iterative training process using known reference energies and forces from electronic structure calculations. No energy partitioning is required as the atomic energies are optimized to yield the correct total energies, which in the present work has been done using the RuNNer code.[46–48] HDNNP energies and forces can be evaluated at about the same computational cost as empirical potentials, enabling the generation of long (and many) trajectories with minimal loss of accuracy. For a comprehensive review on the methodology and construction of HDNNPs we refer the readers to ref. 46 and 47.

2.3.1 **Data set, neural network architecture and global accuracy.** The HDNNP has been parameterized starting from an initial data set of structures that was obtained from three different simulation sources as shown in Table 1. The first, relatively small set consists of single point evaluations at stationary points of the PES and their vicinity. The second and third sets, which represent almost 90% of the final data set, came from *ab initio* MD and PIMD simulations at 150 and 290 K that were performed for the study presented in ref. 2. Because we wanted to extend the range of validity for the HDNNP to higher temperatures, where

Table 1 Description of the data sets available for the construction of the HDNNP. Data sets 1, 2 and 3 were available from a previous work,[2] while data sets 4 and 5 were produced for this study. High temperature simulations refer to additional structures obtained from simulations at 500, 600 and 700 K

Set #	Description	Structures
1	Stationary points set	244
2	Classical MD set	11 033
3	Path integral MD set	80 665
4	High temperature set	7795
5	Umbrella sampling set	2000

different regions of the conformational space can be reached, a fourth set containing structures sampled at 500, 600, and 700 K was included during the training to avoid any type of extrapolation. Finally, to augment the number of data points near the saddle points, 2000 additional structures from an umbrella sampling simulation were added. In total, these two additional sets computed only for this work represent less than 10% of the total data. The data for all 5 different sets was computed with exactly the same numerical settings and level of theory.

We trained seven different HDNNPs with different architectures, data sets and numbers of symmetry functions (SM) (see Table 2). Their overall accuracy is commonly evaluated in terms of the energy and force root mean square error (RMSE) for both training and test sets. Overall, we have been able to reach the typical RMSEs of less than ~1 meV per atom for the energy and less than ~100 meV per Bohr for the force,[47] which are known to yield very good results. We show in Fig. S2 in the ESI† scatter plots comparing DFT energies and HDNNP predictions for points spanning up to 1 eV from the global minimum and append to the ESI† the numerical parameters for all symmetry functions of all NNs.

2.3.2 Validation tests. Since the overall accuracy of all the HDNNPs is comparable, we present the following results as average values calculated from the several trained HDNNPs. In the case of observables involving quantum-nuclear statistics, we exclude the HDNNPs C, D and E because they were not trained explicitly with path integral MD data.

We start our validation tests looking at the stationary points generated by the HDNNP. For this purpose, instead of using the geometries given by DFT, which

Table 2 Architecture, amount of symmetry functions (SM), and overall accuracy for the different trained HDNNPs. Energy and forces RMSEs are expressed in meV per atom and meV per Bohr respectively. We used 2 hidden layers and either 22 or 15 nodes per hidden layer for all elements, as detailed in the architecture field of each network, where G is a placeholder for the number of SM of each element

HDNNP	A	B	C	D	E	F	G
Data set	1, 2, 3, 4	1, 2, 3, 4	1, 2	1, 2, 5	1, 2, 5	1, 2, 3, 4	1, 2, 3, 4, 5
Hydrogen SM	50	50	50	50	72	72	72
Carbon SM	44	44	55	55	72	72	72
Nitrogen SM	40	40	40	40	72	72	72
Architecture	G-22-22-1	G-15-15-1	G-15-15-1	G-15-15-1	G-22-22-1	G-22-22-1	G-22-22-1
Training energy RMSE	1.2	1.5	0.7	0.8	0.6	0.8	1.1
Test energy RMSE	1.5	1.7	0.8	1.0	0.7	1.0	1.2
Training force RMSE	88	99	82	83	72	63	75
Test force RMSE	86	98	83	87	70	62	73

are not necessarily stationary points on the new generated PES, we performed new geometry optimizations for each HDNNP. The results are shown in Table 3 and show an overall overestimation of the energies of ∼5% with respect to the reference values even though the optimized geometries with the HDNNPs are almost identical (see Table SII in ESI†). More interesting are the NH stretch frequencies at those stationary points reported in Table 4. The degree of accuracy observed is remarkable, given that we have not explicitly included any Hessian information during the training procedure.

A considerably more challenging task is the evaluation of the accuracy of the HDNNP on finite-temperature properties of interest. We were in the favorable situation where we had many pre-computed DFT molecular dynamics trajectories at our disposal so we could compare the predictions of the HDNNP and DFT for such properties directly. In Sections II.C and II.D of the ESI† we show these validation tests for quantum-nuclear potential-energy probability densities, VDOS and IR spectra. We find in general that the HDNNP is very accurate for all of these quantities. Small discrepancies appear between ∼600 cm^{-1} and ∼1250 cm^{-1} in the vibrational spectra, and we can connect them to inaccuracies either in the HDNNP potential or in the KRR model for the dipole (described below). Because in this work we will not be focusing in detail on this frequency region, we consider the current setup to be accurate enough for our purposes.

2.4 Dipole surface from kernel ridge regression

Although it is possible to incorporate an approximation to the dipole moment within the HDNN,[49] we here chose to use a KRR model[50] with Gaussian kernels in order to compute the molecular dipole moment of a particular molecular structure. This is a non-linear regression where an l_2-norm regularization is considered in the loss-function, which is then minimized. This method is formally equivalent to a Gaussian Process Regression,[51] but the hyperparameter optimization procedure can differ.

Here we do not make any assumption on the analytical form of the dipole moment, and model each Cartesian component μ_i separately by

$$\mu_i(\mathscr{X}) = \sum_{j=1}^{N_\mathrm{T}} w_j^i K\left(\mathscr{X}, \mathscr{X}_j\right), \tag{4}$$

where the index j runs over the number of points in the training set N_T, w_j^i are the weights, and $K(\mathscr{X}, \mathscr{X}_j) = \mathrm{e}^{-(\mathscr{X} - \mathscr{X}_j)^2/2\sigma^2}$ is the kernel with σ being an hyper-

Table 3 Energy differences at stationary points of the potential energy for DFT and the HDNNP optimized with the respective method, taking as a reference the global minimum *trans* geometry. SD1 and SD2 refer to first and second order saddle points related to the hydrogen-transfer coordinates, respectively. Energies are expressed in meV and the HDNNP energy values are reported as 'mean (standard deviation)' along the HDNNP ensemble. The individual values for each HDNPP are reported in the ESI

	DFT	NN
cis	93	101 (5)
SD1	189	199 (5)
SD2	290	308 (9)

Table 4 NH stretch frequencies for all the stationary points of the potential energy surface for DFT and the HDNNP expressed in cm^{-1}. The NN frequencies are reported as 'mean (standard deviation)' within the HDNNP ensemble. The raw values for each HDNNP are reported in the ESI. SD1 and SD2 refer to first and second order saddle points related to the hydrogen-transfer coordinates, respectively

	DFT	NN
Neg. freq. SD1	1228	1268 (27)
Neg. freq. SD2 (1)	1263	1283 (21)
Neg. freq. SD2 (2)	1126	1153 (33)
N–H *trans*	2903	2917 (15)
N–H *trans*	2907	2929 (14)
N–H *cis*	2678	2644 (40)
N–H *cis*	2640	2673 (64)

parameter which controls the degree of correlation between training points. $\mathscr{X}$ is a vector containing the representation of a particular molecular structure.

By equating the derivative of the loss function to zero, the weights for each dipole component are straightforwardly determined by

$$w^i = (\boldsymbol{K} + \lambda \boldsymbol{I})^{-1} \boldsymbol{\mu}^i(\mathscr{X}), \tag{5}$$

where $\boldsymbol{w}^i = (w_1{}^i, w_2{}^i, \ldots, w_{N_T}{}^i)^T$, $\boldsymbol{\mu}^i = (\mu_1{}^i, \mu_2{}^i, \ldots, \mu_{N_T}{}^i)^T$, $\boldsymbol{K}$ is the kernel covariance matrix, $\boldsymbol{I}$ is the $N_T \times N_T$ identity matrix and the hyperparameter λ sets the strength of the regularization. Both hyperparameters σ and λ are not determined by the previous equation. We determine these parameters through a deterministic grid search, as described below.

The efficiency of most KRR models depends on the representation $\mathscr{X}$ that enters the model. Many groups have proposed strategies to find optimal representation of molecular geometries that can greatly reduce the size of the training set necessary to reach acceptable accuracy.[18,52,53] Symmetry considerations that allow the extension of this model to the prediction of full tensorial quantities of different ranks have also been recently addressed.[54] However, for this work, a very large quantity of data was already available from previous simulations and the system considered here is a relatively rigid molecule. Therefore, we could simply align all geometries and dipole moments to a reference frame and use the Cartesian components as a representation (*i.e.* no representation) to predict each component of the dipole moment separately. The alignment was performed using the following expression

$$y' = R(y)y \tag{6}$$

$$\boldsymbol{\mu}'(y') = R(y)\boldsymbol{\mu}(y) \tag{7}$$

where y and y' are the N Cartesian coordinate vectors of the initial and aligned geometry respectively, N is the number of atoms in the molecule and $\boldsymbol{\mu}$ and $\boldsymbol{\mu}'$ are their corresponding dipole moments. The 3×3 unitary R matrix was obtained with the Kabsch algorithm[55] and has the property of minimizing the root mean squared deviation (RMSD) of the Cartesian coordinates with respect to the reference frame. We have excluded all hydrogen atoms from this procedure.

Table 5 KRR hyperparameters used for each dipole moment component together with the r^2 and ε values obtained for training and test set. All values are reported as an average over the 5 repetitions accompanied by the standard deviation of the mean

	Hyperparameters		Training set		Test set	
	σ (Å)	λ	ε (%)	r^2	ε (%)	r^2
μ_x	3.0	-20	3.74 ± 0.03	0.999 ± 0.001	20.67 ± 0.65	0.957 ± 0.003
μ_y	2.5	-20	1.87 ± 1.19	0.999 ± 0.001	19.14 ± 0.93	0.962 ± 0.004
μ_z	2.5	-19	0.52 ± 0.16	0.999 ± 0.001	3.44 ± 0.12	0.999 ± 0.001

We used a total of ∼9500 data points of which 90% were selected as part of training and the remaining 10% were assigned to the test set. We performed a random selection 5 times in order to obtain statistically meaningful results for the performance of our model. For each division of the data, the hyperparameters σ and λ were determined using the QML package[56] by a grid search minimization of the root mean square error (RMSE) on the test set (see Table 5). As shown in Table 5, the parameters are very similar for all three components, and using the same values for all would result in a minimal difference in the errors.

In order to describe the accuracy of the dipole moment fit, we report in Table 5 the coefficient of determination, r^2, and the RMSE normalized by the standard deviation (STD) $\varepsilon = 100 \times \text{RMSE/STD}$. ε has the advantage of being more sensitive to outliers, in comparison to the mean absolute error, and also allows quantities of different natures to be compared to one another.

Although the errors on the test set are somewhat large (in percentage), they are of a comparable magnitude to what was reported in previous work, that nevertheless could reach the same accuracy with a lesser amount of data and more sophisticated approaches.[54,57] We observe that the models above (with such errors), actually lead to a very good prediction (with smaller errors) of the IR intensities, as shown in Fig. S6 in the ESI.† This effect has also been observed and discussed in ref. 58 for Raman intensities.

2.5 Simulation protocol

All trajectories were computed with HDNNP B using the LAMMPS software[59] and its interface with the RuNNer code.[60] We then used the socket interface between LAMMPS and the i-PI code[61,62] in order to communicate energy and forces to perform classical-nuclei and path-integral molecular dynamics. In order to obtain the TRPMD VDOS, we ran 10 different imaginary path-integral trajectories of 110 ps per temperature, with a time-step of 0.25 fs. The first 10 ps of these runs were discarded as equilibration. We launched a 10 ps long TRPMD trajectory each 10 ps after that. This represents a total amount of 1 ns of statistical sampling per temperature and per isotopologue. In Table 6 we report the number of replicas used for the TRPMD simulations at each temperature.

For classical nuclei simulations, we followed a similar strategy, with the following few differences: (i) since within classical mechanics any time independent equilibrium property is mass independent, we could use the same

Table 6 Number of ring-polymer beads used for each temperature studied

T	50	100	200	300	400
P	256	128	48	32	32

classical-nuclei NVT trajectories for different isotopologues; (ii) we employed a time step of 0.5 fs and (iii) started NVE trajectories from the thermalization run.

In all cases the dipole-moments were obtained *a posteriori* with the KRR model described above, and were calculated at an interval of 2.5 fs.

3 Results and discussion

3.1 Temperature dependent geometrical properties

Geometrical equilibrium properties often have a decisive impact on time dependent properties. In porphycene, a particular geometrical property of interest is the equilibrium N–N distance $d(NN)$ at a given temperature. This is because the dynamics of the hydrogens within the cage are strongly coupled to low frequency modes which modulate the cage size and therefore also $d(NN)$.[63,64]

In Fig. 2(a) we show the average $d(NN)$ as a function of temperature, for the Pc-d0 and Pc-d2 isotopologues, considering quantum and classical nuclei. For classical nuclei simulations, both isotopologues (must) yield the same equilibrium geometrical properties. In all cases, the cage size, reflected by $d(NN)$, increases linearly with temperature. In the temperature range studied, $d(NN)$ of Pc-d0 is smaller than that of Pc-d2 and both are smaller than the classical nuclei $d(NN)$. This geometrical isotope effect (GIE) is the so-called secondary-GIE or the Ubbelohde effect.[65–67] We obtain an almost temperature-independent value of this secondary GIE of 0.016 Å, which compares very well with the experimental inferred one of 0.02 Å.[32] As pointed out by Ubbelohde more than 60 years ago, the "structures may generally be expected to be
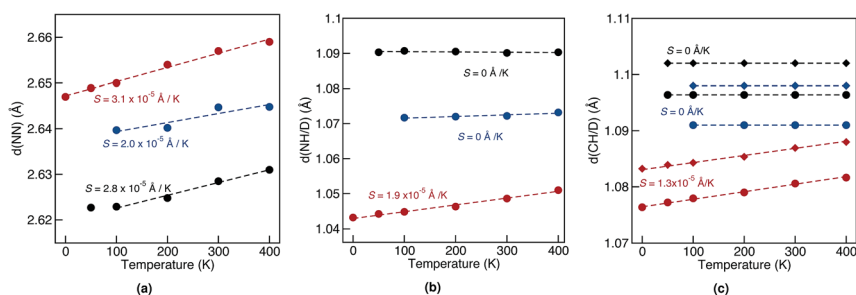

Fig. 2 Average nitrogen–nitrogen (a) and nitrogen–hydrogen/deuterium (b) distances at different temperatures obtained from classical MD (red), and PIMD for Pc-d0 (black) and Pc-d2 (blue) simulations. (c) shows the average carbon–hydrogen/deuterium distances from classical MD (red), and PIMD for Pc-d0 (black) and Pc-d12 (blue). The circles in (c) refer to the eight carbon–hydrogen/deuterium bonds that are part of the pyrrole rings while the diamonds refer to remaining ones. In all cases the statistical error is 0.001 Å or smaller. Dashed lines correspond to linear fits to the data, with the slope S reported in the figure. A value of $S = 0$ means that the observed slope is smaller than the statistical error.

closer for H than for D-bonds, because of differences in zero-point vibra-tions",[65] even though inverse Ubbelohde effects are possible for weak H-bonds, and have been observed.[67,68] In porphycene, where strong directional H-bonds are present, the nuclear-quantum fluctuations along the anharmonic N–H bond increase the N–H bond length $d(NH)$. As shown in Fig. 2(b) this effect is greater for Pc-$d0$ than for Pc-$d2$, which is the so-called primary isotope effect. In both cases, this bond elongation strengthens the H-bond and consequently reduces $d(NN)$, inducing also a correlation between $d(NN)$ and $d(NH/D)$, shown in Fig. 3(a). The similarity of the values of the linear slope S of $d(NN)$ for Pc-$d0$ and Pc-$d2$ above 100 K mean that the cage expansion can be treated classically in this temperature range. At 50 K we observe a deviation from the linear slope for Pc-$d0$, which is consistent with the observation that the lowest cage vibra-tion mode lies at 65 cm^{-1} (≈ 90 K).

The positive sign of S can also be rationalized by analyzing the 1-D PES cut along the $d(NN)$ coordinate shown in Fig. 3(b). The cage modulation is quite anharmonic and the potential is softer towards larger $d(NN)$, such that when more thermal energy is available the average $d(NN)$ will increase. The fact that the cage is much smaller in the quantum case than in the classical case also promotes the population of quasi-*cis* structures that present a permanent dipole, as has been discussed in ref. 2. For the situations above we found that the analysis for Pc-$d12$ is the same as for Pc-$d0$, such that we do not show this data.

For $d(CH/D)$ and $d(NH/D)$ in Fig. 2(b) and (c) we observe no temperature dependence when treating the nuclei quantum mechanically. This is expected, since the frequencies of the corresponding vibrational modes (>1900 cm^{-1}, 2730 K) mean that more than 99.9% of the population stays in the vibrational ground state. In contrast, for classical nuclei the bond elongation increases with temperature even though the coupling between $d(CH/D)/d(NH/D)$ and $d(NN)$ is rather small, as shown in Fig. 3(a). The bond length increase is thus due to the temperature-dependent increase in population of this mode when treated clas-sically and its anharmonic profile. The (quantum) temperature dependence of these geometrical properties for the deuterated isotopologues follows closely the ones for standard porphycene, but the deuterated bonds are always smaller than their hydrogenated counterparts.
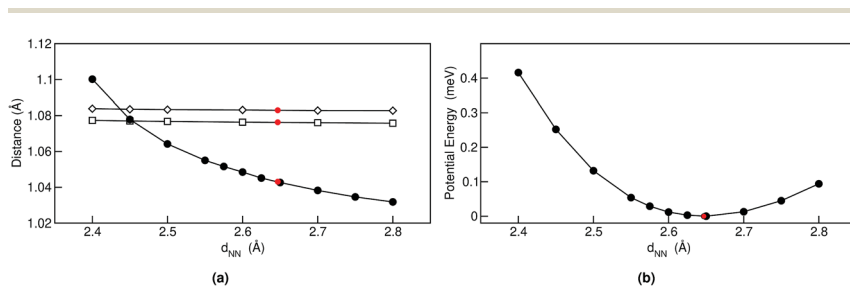

Fig. 3 Selected bond lengths (a) and potential energy (b) for relaxed *trans* structures as a function of nitrogen–nitrogen distance. In (b) the filled circles refer to nitrogen–hydrogen, the empty squares to the eight $d(CH)$ that are connected to the pyrrole rings and the empty diamonds to other $d(CH)$. The red dots represent the values of the fully relaxed structure.

3.2 Temperature-dependent vibrational spectra

Having analyzed the geometrical properties of porphycene and its isotopologues, we turn our attention to vibrational spectra. In Fig. 4 we show the TRPMD VDOS for the three isotopologues in the NH (upper panels) and CH (bottom panels) stretch regions. The full frequency range is reported in the ESI, Fig. S10.† For Pc-*d*0 and Pc-*d*12 (panels a and c), the position and temperature dependence of the NH stretch peak around 2600 cm^{-1} is similar. Importantly, the broadening increases with temperature and it presents an unexpected blue shift of 150 cm^{-1} when the temperature is increased from 50 to 400 K. For Pc-*d*2 (panel b), the ND stretch peak appears at around 2050 cm^{-1}. This value is 200 cm^{-1} above the trivial harmonic mass-scaled frequency, which highlights the anharmonic nature of this vibration. In this case the peak is narrower, and while both the blue shift and the broadening with increasing temperature are still present, their magnitude is smaller if compared to Pc-*d*0.

The CH/D stretch peaks present, for all temperatures and isotopologues, a bimodal distribution emerging from the two types of CH bonds in this molecule: the ones belonging to the pyrrole rings and the ones which are connected to the 'bridge' positions. For the Pc-*d*0 and Pc-*d*2 cases (panels a and b), the CH peaks show a modest blue shift of ~20 cm^{-1} and 10 cm^{-1} when the temperature is increased. On the contrary, the blue shift is not observed for Pc-*d*12 (panel c).

The classical-nuclei VDOS at the same vibrational regions and temperatures are shown in Fig. 5 for Pc-*d*0 (panel a) and Pc-*d*2 (panel b). The full frequency range is reported in the ESI, Fig. S11.† It is clear that, contrary to the TRPMD spectra, the NH and ND-stretch peaks slightly *red*-shift (20 cm^{-1}) with increasing
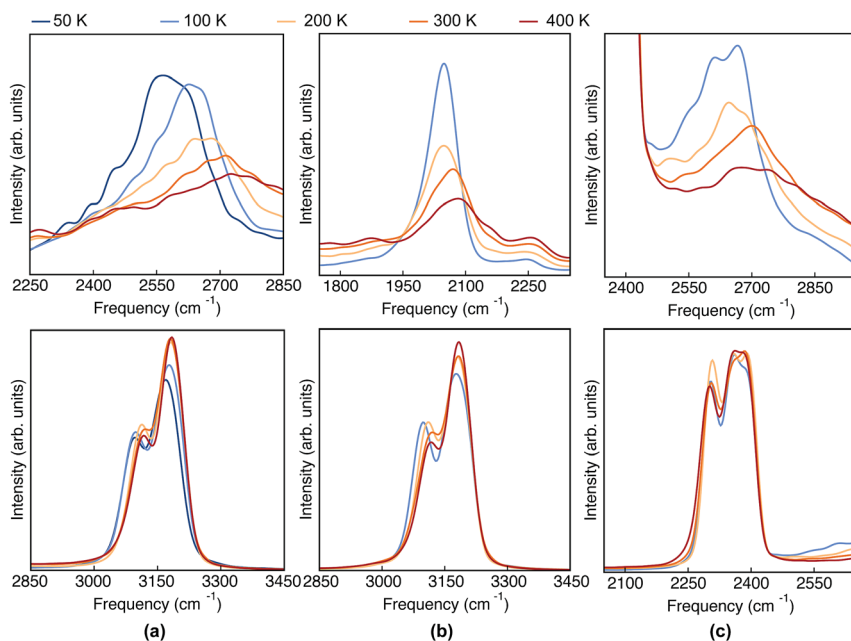

Fig. 4 VDOS obtained from TRPMD simulations at 50 K, 100 K, 200 K, 300 K and 400 K, color coded going from blue (cold) to red (hot) for (a) Pc-*d*0, (b) Pc-*d*2 and (c) Pc-*d*12.
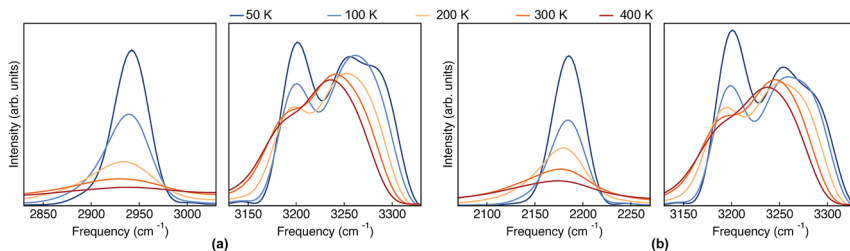
Fig. 5 VDOS obtained from (classical-nuclei) MD simulations at 50 K, 100 K, 200 K, 300 K and 400 K color coded going from blue (cold) to red (hot) for (a) Pc-*d*0 and (b) Pc-*d*2. Note that in this figure the frequency axis spans a range of 200 cm^{-1} while in Fig. 4 it spans a range of 600 cm^{-1}.

temperature. Additionally, these vibrations are situated much closer to the values predicted by the harmonic approximation in this case: 2950 and 2180 cm^{-1} for Pc-*d*0 and Pc-*d*2, respectively. The CH-stretch peaks also consistently red-shift with increasing temperature, and are also situated very close to the harmonic-approximation values of about 3175 and 3250 cm^{-1}.

Clearly, the nature of the high frequency vibrational peaks is strongly affected by nuclear quantum fluctuations, altering both the peak positions and their temperature dependence. In the next section, we explore the physical origins of these effects.

3.2.1 Physical origin of classical and quantum temperature dependence. We now rationalize the stark differences observed in the temperature dependence of the vibrational NH/D and CH/D stretch regions when considering TRPMD and classical nuclei dynamics. As discussed previously, the increase of the temperature induces an expansion of the porphycene cage. Assuming that an adiabatic separation of the high and low frequency modes is valid, we can ask ourselves how the local potential experienced by the NH and CH modes changes with increasing temperature, due to the change in d(NN). In Fig. 6(a) and (b) we show the dependency of the harmonic NH/D and CH/D frequencies with the thermally accessible d(NN) values. We obtained these results by constraining d(NN) at

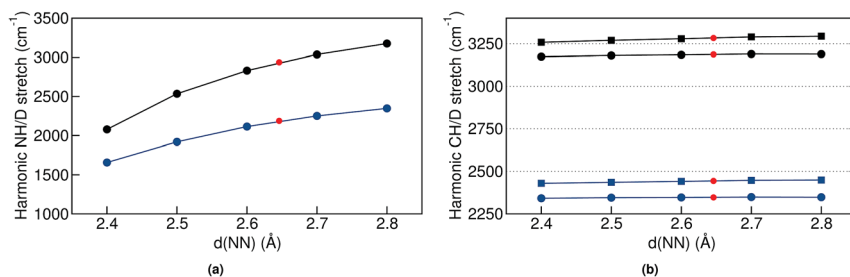**Fig. 6** Selected harmonic stretch frequencies for *trans* structures where all degrees of freedom were optimized except for d(NN). In (a) we show the NH and ND stretch frequencies for Pc-*d*0 (black) and Pc-*d*2 (blue) as a function of d(NN). In (b) we show the CH and CD stretch frequencies for Pc-*d*0 (black) and Pc-*d*12 as a function of d(NN). The red dots represent the values for the relaxed structure.

particular values, relaxing all other degrees of freedom, and then performing a harmonic vibrational analysis. We observe that the harmonic NH stretch frequency (ν_{NH}) spans a range of 1000 cm^{-1} and blue-shifts with increasing $d(NN)$, evidencing the strong coupling of the NH stretch vibration with modes that modulate the cage size. The ND stretch shows the same behavior, but the shift is less pronounced. The CH stretch frequency also blue shifts with increasing $d(NN)$, but only by less than 40 cm^{-1} on the same $d(NN)$ interval and the CD frequency is almost constant.

The simplest model to understand the physics of the NH-stretch potential energy, where exact quantum dynamics can be solved numerically, is a 1D double-well potential that changes with temperature, as shown in Fig. 7. The potential energy surfaces shown there were obtained by calculating the minimum-energy pathway (MEP) projected on the hydrogen-transfer coordinate (see caption of Fig. 7 for a definition of this coordinate). We calculated the MEP for two constrained $d(NN)$ that are representative of the lowest and highest temperatures in this study. The MEP between these two constrained minima was obtained with the nudged elastic band method[69] and it was extended by a harmonic potential at low and high $d(NN)$, consistent with the corresponding NH frequency, in order to model the repulsive parts of the well.

In the classical-nuclei picture, temperature has two important effects. On the one hand, it induces a cage expansion with increasing temperature, and on the other hand, it also increases the thermal population of the NH vibrational well, as pictorially shown in Fig. 7. The first effect makes the walls of the potential increase more steeply with increasing temperature, thus increasing the curvature of the well (blue-shift), as evidenced in Fig. 6(a). The second effect causes the nuclei to explore more anharmonic parts of the well at higher energies, thus causing a red-shift. The final result is a competition between both effects and, for the classical case, the full-dimensional VDOS (Fig. 5) shows that the second one wins at certain temperatures, giving a net red-shift that becomes smaller (and eventually could turn into a blue shift) as the temperature is increased.
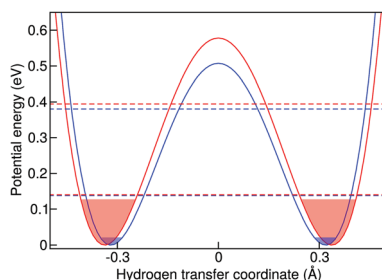

Fig. 7   Model 1D double-well potentials for two fixed $d(NN)$ (see text). Blue and red curves correspond to $d(NN)$ = 2.622 Å and $d(NN)$ = 2.642 Å, respectively. These distances are representative of the $d(NN)$ at 50 and 400 K. Horizontal dashed lines represent the first and second quantum energy levels of each potential. The filled areas show the energies accessible by 98% of the thermal population in a classical picture at 50 K (blue) and 400 K (red). The hydrogen transfer coordinate is defined by the projection of the distance between the hydrogen atom and the middle point of $d(NN)$ into the nitrogen–nitrogen axis. In this way the coordinate is zero when the hydrogen is equidistant to the nitrogen atoms.

In quantum mechanics, however, the situation is quite different. The cage modulation with increasing temperature is similar to the classical-nuclei case. This can be easily understood since the energies of these modes lie at around 200 cm^{-1} (287 K) such that the thermal energy is comparable to the energy level spacing. On the other hand, the NH mode is still completely quantized up to 400 K and its thermal activation is negligible. The ZPE connected to this mode ensures that at all temperatures studied here, the anharmonic parts of the potential are assessed beyond what could be assessed by the classical nuclei simulations, thus explaining the overall red-shift when comparing quantum simulations to the classical ones. However, the insignificant thermal activation in this temperature interval makes this vibration solely sensitive to the modulation of the cage-mode with temperature, such that there is no competition between two effects and the result can only be a blue shift. This effect is also exemplified in Fig. 7. We have calculated the exact quantum mechanical first and second vibrational states connected to the 1D double well potentials presented in the figure, following the algorithm of ref. 70, where the MEP was fitted by a fourth order polynomial in the $[-0.5$ Å, $+0.5$ Å$]$ interval in order to obtain an analytical form of the potential. We show an average of the tunneling-split levels, since these cannot be captured by TRPMD and would be smaller than the temperature broadening at the temperatures studied here. The less-pronounced effect for ND can also be understood within this model, in that the differences between the first vibrational excited state in the two potentials would be smaller.

The 1D potentials shown in Fig. 7 are useful to understand the physics of this problem and the differences between classical and quantum treatment of vibrational degrees of freedom when vibrational coupling between low and high energy modes is present. It also shows that the classical dynamics in the extended phase space of the ring polymer of TRPMD are successful in capturing the main quantum effect that would dictate the temperature dependence of this vibrational peak in full quantum dynamics. However, we find that it is not possible to obtain quantitative results for the observed temperature-dependence of the vibrational frequencies with this simple model. This once more highlights the inherently multi-dimensional nature of this problem.

Finally, for the CH vibrations we observed a much less pronounced blue-shift with increasing temperature. In this case, the CH potential is better described by a Morse potential and perturbative treatments could give reasonable results. We have thus performed second order vibrational perturbation calculations[71,72] (VPT2). They show important couplings between the CH stretch and the CH bending modes. The results reproduce the average peak positions (see Table S4 in the ESI†) that we observe in the TRPMD simulations, and these are all red-shifted with respect to the *harmonic* estimation. However, also this coupling does not immediately explain the blue-shift with increasing temperature, since the bending modes have frequencies starting at 800 cm^{-1}, which correspond only to a 5% thermal population at the highest temperature. We could not find any clear direct coupling between cage modes and the CH stretch, so it is less clear why and how the expansion of the cage modifies the CH-stretch potential. Nevertheless, since the blue shift with increasing d(NN) is very tenuous as shown in Fig. 6(b), for classical nuclei, increasing the thermal population of this mode results in a very pronounced net red shift. For quantum nuclei, again, there is no competition and

we only observe a very small blue shift, which is ~20 times smaller than in the NH case.

3.2.2 Infrared spectra. In order to provide a point of reference for the temperature dependence of vibrational quantities that can be easily accessed in experiment, we report the temperature dependent IR spectra of Pc-$d0$ and Pc-$d2$ above 1600 cm^{-1} in Fig. 8, obtained from TRPMD simulations. The full frequency range and the corresponding results obtained from classical nuclei simulations are reported in the ESI (Fig. S7 and S8†). One point to notice is that compared to full DFT calculations (see ESI† and ref. 2), the IR spectra we obtain with the HDNNP and KRR combination seem to lose some of the fine features present at the combination-band region just below 2000 cm^{-1} for Pc-$d0$, and the fine structure of the NH stretch peak is not so pronounced both in the classical nuclei and the TRPMD simulations. Since both of these features stem from presumably weak mode coupling, we find it plausible that small remaining errors in the models for the forces and in the dipole surface wash out these weak correlations.

As mentioned above, in contrast to the VDOS, the IR spectra contain cross terms involving different nuclei and dipole selection rules. Therefore, lineshapes between VDOS and IR spectra are different and it is not obligatory that trends observed in the VDOS are exactly reflected in the IR spectra. Indeed, the line-shapes in Fig. 8 are different to the VDOS, but the observed temperature depen-dence of the vibrational peaks in this region is very similar to what was discussed for the VDOS. Specifically, Pc-$d0$ presents a blue shift of 100 cm^{-1} and 20 cm^{-1} for NH and CH stretch peak maxima respectively. For Pc-$d2$ the CH blue shift remains comparable (15 cm^{-1}) and the NH one is only 40 cm^{-1}. Both the peak positions and the blue-shifts are larger than what would be predicted by the trivial harmonic isotope $\sqrt{2}$ scaling factor, highlighting once more the anharmonic nature of this problem.

Finally, we comment on the region of the IR spectrum situated between 1750 and 2000 cm^{-1} of Pc-$d0$. The modes in this region are absent in the harmonic spectrum and they are thermally activated in a similar manner (red-shift with increasing temperature) for quantum and classical nuclei. One can thus infer that this band is a combination or overtone of lower-frequency vibrations, as was previously discussed by Gawinkowski and coworkers in ref. 3. The red-shift of 100 cm^{-1} we observe in the TRPMD spectrum is the largest in the whole spectrum (including lower frequencies) and we find the red-shifts of the bands situated between 800 and 1000 cm^{-1} to be more consistent with the combined shift, thus pointing to overtones. We could not further analyze our results at this point in order confirm this interpretation.
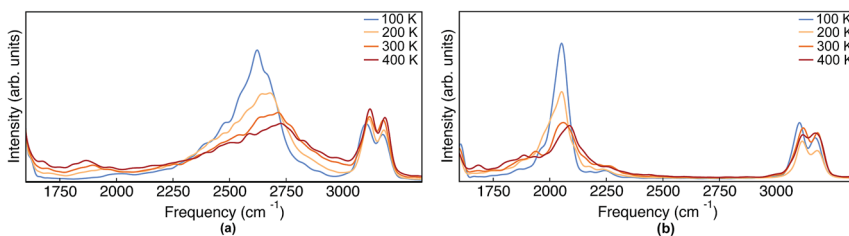

Fig. 8 IR spectra obtained from TRPMD simulations of (a) Pc-$d0$ and (b) Pc-$d2$ at 100 K, 200 K, 300 K and 400 K.

4   Concluding remarks

In this work we have studied the temperature dependence of structural and vibrational properties of the gas-phase porphycene molecule and its iso-topologues, namely Pc-$d0$, Pc-$d2$ and Pc-$d12$, in temperatures ranging from 50 to 400 K. We employed high-dimensional neural-network potentials trained on B3LYP + vdW data to calculate energy and forces, augmented by a kernel ridge regression model for the dipole surface. We took nuclear quantum effects into account through imaginary-time path integral and thermostatted ring polymer molecular dynamics.

We could explain the primary and secondary geometric isotope effects related to the N–N and N–H/D distances, and found good agreement with experiment. The strong hydrogen bonds within the cage are strengthened by nuclear quantum effects, such that the N–N distances are larger for Pc-$d2$ than for Pc-$d0$, while the N–H/D distances are smaller for Pc-$d2$ than for Pc-$d0$. In all cases the cage of porphycene expands with increasing temperature.

Regarding vibrational properties of Pc-$d0$, we find that anharmonic vibrational spectra derived from classical-nuclei molecular dynamics show a red-shift of both NH and CH stretch regions with increasing temperature. Approximate quantum dynamics (TRPMD) instead predicts a pronounced blue-shift (150 cm^{-1}) in the NH stretch region with increasing temperature and a small blue-shift in the CH stretch region. For Pc-$d2$, the ND stretch shows a less pronounced blue-shift and for Pc-$d12$ the CD stretch region remains unchanged throughout this temperature range.

The temperature behavior of the NH(ND) stretch regions is a consequence of vibrational coupling between quasi-classical thermally activated cage expansion/contraction modes and high-frequency quantized modes. We could understand the underlying physics of the problem by analyzing a 1D double-well model where the distance (and the barrier height) between the two wells increases with temperature. In classical mechanics there is a competition between the increasing thermal population of the well and the increasing curvature of the potential as the temperature increases. The first causes a red-shift due to the anharmonicity of the potential, while the second causes a blue-shift due to the effective decrease of anharmonicity at the bottom of the well. In quantum mechanics, at all temperatures studied here, the thermal population of excited vibrational states is completely negligible, such that only the modulation of the potential with temperature plays a role and the result is a pronounced blue shift. The approximate quantum dynamics of TRPMD are able to grasp this effect, because ZPE is correctly described at the different temperatures and the linear-response transition probabilities are only sensitive to the stiffening in the effective curvature of the potential with increasing temperature. Even though the 1D model in this case is useful to understand the underlying physics, no quantitative predictions could be achieved with it, highlighting the inherent high-dimensionality of the problem.

For the CH/D stretch regions the direct coupling between low and high frequency modes is less clear, but we observe the that the cage expansion is correlated to a blue shift with increasing temperature. We note that the (quantum) blue-shift with increasing temperature observed for this isolated gas-

phase molecule seems not to have the same origin as the ones observed in condensed phase systems,[11,13,73] where it is understood that the shifts are due to the weakening of intermolecular H-bonds with increasing temperature.

In summary, we have shown that the porphycene molecule is a clear example where considering nuclei as classical particles makes the theory inaccurate and completely removes its predictive power for a range of geometrical and vibrational properties. On the other hand, path-integral based approximations to quantum dynamics, which conserve the quantum Boltzmann distribution and therefore are free from ZPE leakage, are able to grasp the correct underlying physics in this system. In fact, even though we treated an isolated molecule here, the large amount of (anharmonic) degrees of freedom and the temperature range considered washes out most dynamical quantum coherence effects, which presents an ideal ground for such methods. We have also demonstrated that when a large amount of data from *ab initio* simulations is available, the effort to train high dimensional neural network potentials and kernel ridge regression models that accurately reproduce energy, forces and dipoles can be minimal. This makes it possible to address new physical problems that would be too cost-intensive with accurate DFT potentials – in particular, problems that take the quantum nature of nuclei into account. Open access data repositories that can handle, specifically, data related to *ab initio* molecular dynamics trajectories will be paramount to make this approach more common in the near future.

Conflicts of interest

There are no conflicts to declare.

Acknowledgements

References

1 J. Waluk, *Chem. Rev.*, 2017, **117**, 2447–2480.
2 Y. Litman, J. O. Richardson, T. Kumagai and M. Rossi, *J. Am. Chem. Soc.*, 2019, **141**, 2526–2534.
3 S. Gawinkowski, L. Walewski, A. Vdovin, A. Slenczka, S. Rols, M. R. Johnson, B. Lesyng and J. Waluk, *Phys. Chem. Chem. Phys.*, 2012, **14**, 5489–5503.
4 P. Fita, L. Grill, A. Listkowski, H. Piwonski, S. Gawinkowski, M. Pszona, J. Sepiol, E. Mengesha, T. Kumagai and J. Waluk, *Phys. Chem. Chem. Phys.*, 2017, **19**, 4921–4937.
5 J. Kügel, M. Leisegang and M. Bode, *ACS Nano*, 2018, **12**, 8733–8738.

6 J. Kügel, M. Leisegang, M. Böhme, A. Krönlein, A. Sixta and M. Bode, *Nano Lett.*, 2017, **17**, 5106–5112.

7 H. Böckmann, S. Liu, J. Mielke, S. Gawinkowski, J. Waluk, L. Grill, M. Wolf and T. Kumagai, *Nano Lett.*, 2016, **16**, 1034–1041.

8 T. Kumagai, F. Hanke, S. Gawinkowski, J. Sharp, K. Kotsis, J. Waluk, M. Persson and L. Grill, *Phys. Rev. Lett.*, 2013, **111**, 246101.

9 J. N. Ladenthin, T. Frederiksen, M. Persson, J. C. Sharp, S. Gawinkowski, J. Waluk and T. Kumagai, *Nat. Chem.*, 2016, **8**, 935–940.

10 T. Kumagai, J. N. Ladenthin, Y. Litman, M. Rossi, L. Grill, S. Gawinkowski, J. Waluk and M. Persson, *J. Chem. Phys.*, 2018, **148**, 102330.

11 F. Paesani, *J. Phys. Chem. A*, 2011, **115**, 6861–6871.

12 S. K. Reddy, D. R. Moberg, S. C. Straight and F. Paesani, *J. Chem. Phys.*, 2017, **147**, 244504.

13 T. Morawietz, O. Marsalek, S. R. Pattenaude, L. M. Streacker, D. Ben-Amotz and T. E. Markland, *J. Phys. Chem. Lett.*, 2018, **9**, 851–857.

14 Y. C. Shen, P. C. Upadhya, E. H. Linfield and A. G. Davies, *Appl. Phys. Lett.*, 2003, **82**, 2350–2352.

15 E. Garrone and C. Otero Areán, *Chem. Soc. Rev.*, 2005, **34**, 846–857.

16 J. Behler, *Phys. Chem. Chem. Phys.*, 2011, **13**, 17930–17955.

17 J. Behler, *J. Chem. Phys.*, 2016, **145**, 170901.

18 A. P. Bartók and G. Csányi, *Int. J. Quantum Chem.*, 2015, **115**, 1051–1057.

19 V. Botu, R. Batra, J. Chapman and R. Ramprasad, *J. Phys. Chem. C*, 2017, **121**, 511–522.

20 S. Chmiela, A. Tkatchenko, H. E. Sauceda, I. Poltavsky, K. T. Schütt and K. R. Müller, *Sci. Adv.*, 2017, **3**, 1–6.

21 M. Ceriotti, *J. Chem. Phys.*, 2019, **150**, 150901.

22 M. Rupp, *Int. J. Quantum Chem.*, 2015, **115**, 1058–1073.

23 J. Behler and M. Parrinello, *Phys. Rev. Lett.*, 2007, **98**, 146401.

24 J. Behler, *J. Chem. Phys.*, 2011, **134**, 074106.

25 A. D. Becke, *J. Chem. Phys.*, 1993, **98**, 5648–5652.

26 C. Lee, W. Yang and R. G. Parr, *Phys. Rev. B: Condens. Matter Mater. Phys.*, 1988, **37**, 785–789.

27 S. H. Vosko, L. Wilk and M. Nusair, *Can. J. Phys.*, 1980, **58**, 1200–1211.

28 P. J. Stephens, F. J. Devlin, C. F. Chabalowski and M. J. Frisch, *J. Phys. Chem.*, 1994, **98**, 11623–11627.

29 A. Tkatchenko and M. Scheffler, *Phys. Rev. Lett.*, 2009, **102**, 073005.

30 P. Ciacka, P. Fita, A. Listkowski, C. Radzewicz and J. Waluk, *J. Phys. Chem. Lett.*, 2016, **7**, 283–288.

31 E. T. Mengesha, A. Zehnacker-Rentien, J. Sepioł, M. Kijak and J. Waluk, *J. Phys. Chem. B*, 2015, **119**, 2193–2203.

32 M. F. Shibl, M. Pietrzak, H. H. Limbach and O. Kühn, *ChemPhysChem*, 2007, **8**, 315–321.

33 T. Yoshikawa, S. Sugawara, T. Takayanagi, M. Shiga and M. Tachikawa, *Chem. Phys.*, 2012, **394**, 46–51.

34 V. Blum, R. Gehrke, F. Hanke, P. Havu, V. Havu, X. Ren, K. Reuter and M. Scheffler, *Comput. Phys. Commun.*, 2009, **180**, 2175–2196.

35 D. A. McQuarrie, *Statistical mechanics*, University Science Books, 2000.

36 C. James, *Structural Chemistry of Glasses*, Elsevier Science Ltd, Oxford, 2002, pp. 137–183.

37 R. Zwanzig, *Phys. Rev.*, 1964, **133**, A50–A51.

38 B. J. Braams, T. F. Miller III and D. E. Manolopoulos, *Chem. Phys. Lett.*, 2006, **418**, 179–184.

39 S. Habershon, B. J. Braams and D. E. Manolopoulos, *J. Chem. Phys.*, 2007, **127**, 174108.

40 M. Rossi, M. Ceriotti and D. E. Manolopoulos, *J. Chem. Phys.*, 2014, **140**, 234116.

41 I. R. Craig and D. E. Manolopoulos, *J. Chem. Phys.*, 2004, **121**, 3368–3373.

42 T. J. H. Hele, M. J. Willatt, A. Muolo and S. C. Althorpe, *J. Chem. Phys.*, 2015, **142**, 134103.

43 T. J. H. Hele, M. J. Willatt, A. Muolo and S. C. Althorpe, *J. Chem. Phys.*, 2015, **142**, 191101.

44 T. J. H. Hele, *Mol. Phys.*, 2016, **114**, 1461–1471.

45 M. Rossi, V. Kapil and M. Ceriotti, *J. Chem. Phys.*, 2018, **148**, 102301.

46 J. Behler, *Int. J. Quantum Chem.*, 2015, **115**, 1032–1050.

47 J. Behler, *Angew. Chem., Int. Ed.*, 2017, **56**, 12828.

48 J. Behler, *RuNNer - A Neural Network Code for High-Dimensional Potential-Energy Surfaces*, Universität Göttingen, 2018, http://www.uni-goettingen.de/de/560580.html.

49 M. Gastegger, J. Behler and P. Marquetand, *Chem. Sci.*, 2017, **8**, 6924.

50 T. Hastie, R. Tibshirani and J. Friedman, *The Elements of Statistical Learning*, 2nd edn, Springer, New York, 2009.

51 C. E. Rasmussen and C. K. I. Williams, *Gaussian Processes for Machine Learning*, MIT Press, 2006.

52 H. Huo and M. Rupp, arXiv:1704.06439, 2017.

53 M. Rupp, A. Tkatchenko, K. R. Müller and O. A. von Lilienfeld, *Phys. Rev. Lett.*, 2012, **108**, 058301.

54 A. Grisafi, D. M. Wilkins, G. Csányi and M. Ceriotti, *Phys. Rev. Lett.*, 2018, **120**, 036002.

55 W. Kabsch, *Acta Crystallogr., Sect. A: Cryst. Phys., Diffr., Theor. Gen. Crystallogr.*, 1978, **34**, 827–828.

56 A. S. Christensen, F. A. Faber, B. Huang, L. Bratholm, A. Tkatchenko, K. R. Muller and O. A. von Lilienfeld, *QML: A Python Toolkit for Quantum Machine Learning*, https://github.com/qmlcode/qml.

57 M. J. Willatt, F. Musil and M. Ceriotti, *J. Chem. Phys.*, 2019, **150**, 154110.

58 N. Raimbault, A. Grisafi, M. Ceriotti and M. Rossi, *New J. Phys.*, 2019, DOI: 10.1088/1367-2630/ab4509.

59 S. Plimpton, *J. Comput. Phys.*, 1995, **117**, 1.

60 A. Singraber, J. Behler and C. Dellago, *J. Chem. Theory Comput.*, 2019, **15**, 1827–1840.

61 V. Kapil, M. Rossi, O. Marsalek, R. Petraglia, Y. Litman, T. Spura, B. Cheng, A. Cuzzocrea, R. H. Meißner, D. M. Wilkins, B. A. Helfrecht, P. Juda, S. P. Bienvenue, W. Fang, J. Kessler, I. Poltavsky, S. Vandenbrande, J. Wieme, C. Corminboeuf, T. D. Kühne, D. E. Manolopoulos, T. E. Markland, J. O. Richardson, A. Tkatchenko, G. A. Tribello, V. V. Speybroeck and M. Ceriotti, *Comput. Phys. Commun.*, 2019, **236**, 214–223.

62 M. Ceriotti, J. More and D. E. Manolopoulos, *Comput. Phys. Commun.*, 2014, **185**, 1019–1026.

63 M. F. Shibl, M. Tachikawa and O. Kühn, *Phys. Chem. Chem. Phys.*, 2005, 7, 1368–1373.

64 M. Gil and J. Waluk, *J. Am. Chem. Soc.*, 2007, **129**, 1335–1341.

65 A. R. Ubbelohde and K. J. Gallagher, *Acta Crystallogr.*, 1955, **8**, 71–83.

66 H. Benedict, H. H. Limbach, M. Wehlan, W.-P. Fehlhammer, N. S. Golubev and R. Janoschek, *J. Am. Chem. Soc.*, 1998, **120**, 2939–2950.

67 X. Z. Li, B. Walker and A. Michaelides, *Proc. Natl. Acad. Sci. U. S. A.*, 2011, **108**, 6369–6373.

68 H.-H. L. A. Kohen, *Isotope Effects In Chemistry and Biology*, CRC Press, 2005.

69 G. Henkelman and H. Jónsson, *J. Chem. Phys.*, 2000, **113**, 9978–9985.

70 D. T. Colbert and W. H. Miller, *J. Chem. Phys.*, 1992, **96**, 1982–1991.

71 S. Califano, *Vibrational States*, John Wiley & Sons, 1976, pp. 266–302.

72 V. Barone, *J. Chem. Phys.*, 2005, **122**, 014108.

73 Y. Katsumoto, H. Komatsu and K. Ohno, *J. Am. Chem. Soc.*, 2006, **128**, 9278–9279.